

Microseismicity and lithosphere thickness at a nearly amagmatic mid-ocean ridge

Jie Chen (✉ chenjie.geo@outlook.com)

Université de Paris, Institut de physique du globe de Paris, CNRS <https://orcid.org/0000-0002-4674-8351>

Wayne Crawford

Institut de Physique du Globe de Paris

Mathilde Cannat

IPGP - CNRS UMR 7135

Article

Keywords:

Posted Date: December 6th, 2021

DOI: <https://doi.org/10.21203/rs.3.rs-1046015/v1>

License: © ⓘ This work is licensed under a Creative Commons Attribution 4.0 International License.

[Read Full License](#)

Microseismicity and lithosphere thickness at a nearly amagmatic mid-ocean ridge

Jie Chen, Wayne C. Crawford, Mathilde Cannat

Université de Paris, Institut de physique du globe de Paris, CNRS, F-75005 Paris, France

Correspondence author: Jie Chen (chenjie.geo@outlook.com)

Successive flip-flop detachment faults in a nearly-amagmatic region of the ultraslow-spreading Southwest Indian Ridge (SWIR) at 64°30'E accommodate ~100% of plate divergence, with mostly ultramafic seafloor. As magma is the main heat carrier to the oceanic lithosphere, the nearly-amagmatic SWIR 64°30'E is expected to have a very thick lithosphere. Here, our microseismicity data shows a 15-km thick seismogenic lithosphere, actually thinner than the more magmatic SWIR Dragon Flag detachment with the same spreading rate. This challenges current models of how spreading rate and melt supply control the thermal regime of mid-ocean ridges. Microearthquakes with normal focal mechanisms are colocated with seismically imaged damage zones of the detachment and reveal hanging-wall normal faulting, which is not seen at more magmatic detachments at the SWIR or the Mid-Atlantic Ridge. We also document a two-day seismic swarm, interpret as caused by an upward-migrating melt intrusion in the detachment footwall (6-11 km), triggering a sequence of shallower (~1.5 km) tectonic earthquakes in the detachment fault plane. This points to a possible link between sparse magmatism and tectonic failure at melt-poor ultraslow ridges.

A successive flip-flop detachment fault system discovered at a nearly-amagmatic region of the ultraslow spreading Southwest Indian Ridge (SWIR; full spreading rate of 14 mm/yr) at 64°30'E reveals a previously unknown seafloor spreading mode¹⁻³ (Fig. 1a). In this mode, the detachments accommodate nearly 100% of plate divergence, continuously cutting into the footwalls of their predecessors, with flipping polarities every 0.6-1.5 Ma^{1,2} (Fig. 1). The resulting seafloor morphology is the so-called smooth seafloor⁴, with extensive exposure of mantle-derived peridotites and only patches of hummocky basalts². This newly-discovered seafloor spreading mode differs from the "classic" detachment-volcanic and volcanic-volcanic modes at slow spreading ridges and at more magmatically-robust portions of ultraslow spreading ridges, where at least one plate is dominated by abyssal-hill volcanic seafloor⁴⁻¹⁰.

Seismicity provides a means to study magmatic, tectonic, and hydrothermal processes within the lithosphere of mid-ocean ridges¹¹⁻¹⁷ (MORs), and is an indirect proxy for the thermal regime by constraining the depth to the base of the seismogenic lithosphere^{18,19}. The thickness of the axial seismogenic lithosphere is numerically predicted to increase as spreading rate decreases¹⁸ and/or as melt supply decreases²⁰. The ultraslow spreading SWIR 64°30'E, being nearly amagmatic, may be regarded as a geothermal calibration for the MOR system.

In this study, we present 309 microearthquakes and 8 focal mechanisms associated with the youngest, active detachment system (DF1) at the SWIR 64°30'E (Methods), as recorded during two short (8 days for the SMSMO catalog and 19 days for the RVSMO catalog) ocean bottom seismometer (OBS) deployments (Figs. 1 and 2a). Our results demonstrate tectonic activities at the detachment damage zones and provide constraints on the thickness of the seismogenic lithosphere. We also document a two-day seismic swarm which we propose is related to the incipient volcanism witnessed by patches of hummocky basalts resting on the

ultramafic seafloor.

Results and discussion

Seismicity of the detachment fault system

The two short OBS deployments we report on offer snapshots in time of the seismic activity. Most microearthquakes occurred in the axial valley (Fig. 2a) between the emergence of DF1 (E1) and the breakaway of DF2 (B2), with an average seismicity rate of 11.4 events per day (8.4 and 12.7 events per day in the SMSMO and RVSMO catalogs, respectively). The highest number of events is recorded near the longitude of the P2-P2' profile, and there is an apparent seismic gap to the west of the P1-P1' profile (Figs. 2a and 2c). Earthquake hypocenters have depths between 0 and 15 km below the seafloor (bsf), and events in the shorter SMSMO catalog were mostly at less than 10 km bsf (Fig. 2b). Local magnitudes (M_L) range from -0.5 to 3.2, with a magnitude of completeness of 1.1 and a b-value of 0.9 based on the Gutenberg-Richter relation²¹ (Methods and Extended Data Fig. 6). Focal mechanisms correspond to normal faulting, as expected in an extensional context, except for one strike-slip faulting event (Fig. 2a).

Many microearthquake hypocenters plotted in the cross-axis sections P1-P1' and P2-P2' (Figs. 2d and 2e) are aligned with the trace of the subseafloor detachment fault plane as inferred from a series of subparallel seismic reflectors with a dip of 50-60°^{22,23}. In the three profiles, and particularly along P3-P3', there are several events scattered in the detachment footwall and hanging wall. This differs from the seismicity recorded at more magmatically active detachment systems, such as the 13°20'N, TAG, and Logatchev detachment faults at the Mid-Atlantic Ridge^{14,17,24,25} and the Dragon Flag detachment fault of the SWIR^{26,27}, where there are very few earthquakes in the hanging wall. Focal mechanisms of the hanging-wall earthquakes display a prevalence of normal faults with an average dip of 50° at 2-7 km

bsf (Figs. 2e and 2f). These dips are consistent with the geometry of nearby north-dipping seismic reflectors²² (Fig. 2f) and with small-offset fault scarps at the seafloor², suggesting that these small faults are conjugate with the detachment fault.

We also observe a larger number of earthquakes in the detachment damage zone and in the hanging wall, at the transition between volcanic and smooth seafloor (Figs. 2c and 2e), where intrusive magmatic sills were proposed to explain subhorizontal seismic reflectors²³. Due to the low friction coefficients associated with partial serpentinization, the brittle ultramafic basement may be less prone to seismogenic rupture than the more competent crystallized basalts or gabbros. Our observations may thus provide a framework to examine earthquake generation at detachment systems, interacting with sparse magmatism.

Thickness of seismogenic lithosphere and the axial thermal regime

The microearthquakes constrain the thickness of the seismogenic lithosphere to be at least 15 km in this nearly-amagmatic, ultraslow spreading MOR context (Fig. 2b), and this thickness is mostly uniform along the ridge axis, across the transition from smooth to volcanic seafloor (Fig. 2c). The thickness of the seismogenic lithosphere is believed to be mainly controlled by the thermal regime, with its base roughly corresponding to the 650°C isotherm^{19,28,29}. This is consistent with the minimum depth of 18 km bsf and 800 to 1000°C temperature conditions, determined from petrological constraints for the high-stress ductile deformation of sheared peridotites dredged in the same area^{30,31}. A greater maximum depth of microearthquakes (>20 km) was documented at the adjacent magma-poor SWIR 65°10'E³², but these deep earthquakes are well outside the OBS network (>10 km) and were located using a velocity model derived from the magmatically-robust segment #8 volcano³³ (Methods and Supplementary Fig. 1), which could bias their depths.

At slow spreading ridges detachments, the maximum depth of earthquakes reaches 6-7

km bsf at the MAR 14°75'N and TAG^{17,25} and 12 km bsf at the MAR 13°N^{14,24}. At ultraslow spreading ridges, this depth reaches 17-18 km at the Knipovich Ridge and at the SWIR 13°E^{34,35}, where highly oblique spreading produces effective spreading rates of only 7-8 mm/yr. Seismic events are reported down to 18 km bsf at the magmatically-robust Dragon Flag detachment system^{26,27} (Methods) and 10 km bsf at the Mount Dent detachment of the Mid-Cayman Spreading Center³⁵. Intriguingly, the more magmatically-robust Dragon Flag has a seismogenic lithosphere that is equivalent or greater in thickness to that determined here for the nearly-amagmatic SWIR 64°30'E with the same spreading rate. This questions current numerical models of the links between spreading rate, melt supply, and the thermal regime of the MOR^{18,20}. We propose that hydrothermal removal of magmatic heat at Dragon Flag may be more efficient than modelled, as evidenced by numerous black smokers^{36,37}.

Seismicity induced by melt intrusions in the ultramafic basement

A swarm of 34 earthquakes with a mean M_L of 0.9 and no identifiable mainshock was observed at the transition between volcanic and smooth seafloor in the RVSMO catalog during Dec 22-23, 2016 (Figs. 3a and 3b). We did not obtain well-constrained focal mechanisms due to the lesser number of OBSs in the RVSMO deployment (Methods). Earthquakes of this swarm are divided into three nearly simultaneous clusters based on spatial distribution: deep-west (14 events), deep-east (8 events), and shallow (12 events). The deep-west and deep-east clusters occurred 6 to 11 km into the detachment footwall (Fig. 3c). The shallow cluster was concentrated at ~1.5 km bsf near the detachment fault (Fig. 3c). All three clusters extend 1 to 2 km in the east-west, along-axis direction, with no lateral migration of the activity in time within each cluster. The swarm initiated in the deep-west cluster, with events starting in the other two clusters within 6 hours. The last 3 events of the deep-west cluster are located upward and to the north (Figs. 3b and 3c), indicating an upward migration of activity by about 2 km during the last ~8 hours of the migration (Figs. 3b and

3c). This, and its location underneath the volcanic hummocky seafloor (Fig. 3b), leads us to interpret this deep-west cluster as related to a magma injection. The nature of the deep-east cluster is not clear, but it is expected for a melt injection in this extensional context. The near-fault location of the shallow cluster and the lack of events joining it to the deeper events lead us to propose that the shallow cluster is tectonic. The swarm may thus be of mixed magmatic and tectonic origins, with tectonic activity at ~1.5 km bsf in the detachment being triggered by a magma injection at 11 to 6 km bsf in the detachment footwall. This could mean that melt intruding into the brittle peridotites at depths altered the stresses in the detachment footwall, so that a shallow portion of the fault which was near to rupture broke.

References

1. Cannat, M. *et al.* On spreading modes and magma supply at slow and ultraslow mid-ocean ridges. *Earth Planet. Sci. Lett.* **519**, 223–233 (2019).
2. Sauter, D. *et al.* Continuous exhumation of mantle-derived rocks at the Southwest Indian Ridge for 11 million years. *Nat. Geosci.* **6**, 314–320 (2013).
3. Reston, T. Flipping detachments: The kinematics of ultraslow spreading ridges. *Earth Planet. Sci. Lett.* **503**, 144–157 (2018).
4. Cannat, M. *et al.* Modes of seafloor generation at a melt-poor ultraslow-spreading ridge. *Geology* **34**, 605–608 (2006).
5. Escartín, J. *et al.* Central role of detachment faults in accretion of slow-spreading oceanic lithosphere. *Nature* **455**, 790–794 (2008).
6. Buck, W. R., Lavier, L. L. & Poliakov, A. N. B. Modes of faulting at mid-ocean ridges. *Nature* **434**, 719–723 (2005).
7. Smith, D. K., Escartín, J., Schouten, H. & Cann, J. R. Fault rotation and core complex formation: Significant processes in seafloor formation at slow-spreading mid-ocean ridges (Mid-Atlantic Ridge, 13°–15°N). *Geochemistry, Geophys. Geosystems* **9**, (2008).
8. MacLeod, C. J. *et al.* Life cycle of oceanic core complexes. *Earth Planet. Sci. Lett.* **287**, 333–344 (2009).
9. Olive, J. A. & Dublanchet, P. Controls on the magmatic fraction of extension at mid-ocean ridges. *Earth Planet. Sci. Lett.* **549**, 116541 (2020).
10. Tucholke, B. E., Behn, M. D., Buck, W. R. & Lin, J. Role of melt supply in oceanic detachment faulting and formation of megamullions. *Geology* **36**, 455–458 (2008).
11. Meier, M. & Schlindwein, V. First In Situ Seismic Record of Spreading Events at the Ultraslow Spreading Southwest Indian Ridge. *Geophys. Res. Lett.* **45**, 10,360–10,368

- 154 (2018).
- 155 12. Kong, L. S. L., Solomon, S. C. & Purdy, G. M. Microearthquake characteristics of a
156 mid-ocean ridge along-axis high. *J. Geophys. Res.* **97**, (1992).
- 157 13. Tilmann, F., Flueh, E., Planert, L., Reston, T. & Weinrebe, W. Microearthquake
158 seismicity of the Mid-Atlantic Ridge at 5°S: A view of tectonic extension. *J. Geophys.*
159 *Res. Solid Earth* **109**, (2004).
- 160 14. Parnell-Turner, R. *et al.* Oceanic detachment faults generate compression in extension.
161 **45**, (2017).
- 162 15. Tan, Y. J., Tolstoy, M., Waldhauser, F. & Wilcock, W. S. D. Dynamics of a seafloor-
163 spreading episode at the East Pacific Rise. *Nature* **540**, 261–265 (2016).
- 164 16. Pontbriand, C. W. & Sohn, R. A. Microearthquake evidence for reaction-driven
165 cracking within the Trans-Atlantic Geotraverse active hydrothermal deposit. *J.*
166 *Geophys. Res. Solid Earth* **119**, (2014).
- 167 17. de Martin, B. J., Reves-Sohn, R. A., Canales, J. P. & Humphris, S. E. Kinematics and
168 geometry of active detachment faulting beneath the Trans-Atlantic geotraverse (TAG)
169 hydrothermal field on the Mid-Atlantic Ridge. *Geology* **35**, 711–714 (2007).
- 170 18. Phipps Morgan, J. & Chen, Y. J. Dependence of ridge-axis morphology on magma
171 supply and spreading rate. *Nature* **364**, 706–708 (1993).
- 172 19. McKenzie, D., Jackson, J. & Priestley, K. Thermal structure of oceanic and continental
173 lithosphere. *Earth Planet. Sci. Lett.* **233**, (2005).
- 174 20. Fan, Q., Olive, J. A. & Cannat, M. Thermo-Mechanical State of Ultraslow-Spreading
175 Ridges With a Transient Magma Supply. *J. Geophys. Res. Solid Earth* **126**,
176 e2020JB020557 (2021).
- 177 21. Gutenberg, B. & Richter, C. F. Frequency of earthquakes in California. *Bull. Seismol.*
178 *Soc. Am.* **34**, 185–188 (1944).
- 179 22. Momoh, E., Cannat, M., Watremez, L., Leroy, S. & Singh, S. C. Quasi-3-D Seismic
180 Reflection Imaging and Wide-Angle Velocity Structure of Nearly Amagmatic Oceanic
181 Lithosphere at the Ultraslow-Spreading Southwest Indian Ridge. *J. Geophys. Res.*
182 *Solid Earth* **122**, 9511–9533 (2017).
- 183 23. Momoh, E., Cannat, M. & Leroy, S. Internal Structure of the Oceanic Lithosphere at a
184 Melt-Starved Ultraslow-Spreading Mid-Ocean Ridge: Insights From 2-D Seismic
185 Data. *Geochemistry, Geophys. Geosystems* **21**, (2020).
- 186 24. Parnell-Turner, R. *et al.* Seismicity trends and detachment fault structure at 13°N,
187 Mid-Atlantic Ridge. *Geology* XXX–XXX (2020) doi:10.1130/g48420.1.
- 188 25. Grevenmeyer, I., Reston, T. J. & Moeller, S. Microseismicity of the Mid-Atlantic Ridge
189 at 7°S–8°15'S and at the Logatchev Massif oceanic core complex at 14°40'N– 14°50'N.
190 *Geochemistry, Geophys. Geosystems* **14**, 3532–3554 (2013).
- 191 26. Tao, C. *et al.* Deep high-temperature hydrothermal circulation in a detachment faulting
192 system on the ultra-slow spreading ridge. *Nat. Commun.* **11**, 1–9 (2020).
- 193 27. Yu, Z. *et al.* Lithospheric Structure and Tectonic Processes Constrained by
194 Microearthquake Activity at the Central Ultraslow-Spreading Southwest Indian Ridge
195 (49.2° to 50.8°E). *J. Geophys. Res. Solid Earth* **123**, 6247–6262 (2018).
- 196 28. Anderson, D. L. Lithosphere, asthenosphere, and perisphere. *Reviews of Geophysics*

- 197 vol. 33 (1995).
- 198 29. Wang-Pin Chen & Molnar, P. Focal depths of intracontinental and intraplate
199 earthquakes and their implications for the thermal and mechanical properties of the
200 lithosphere. *J. Geophys. Res.* **88**, (1983).
- 201 30. Bickert, M., Cannat, M., Tommasi, A., Jammes, S. & Lavier, L. Strain Localization in
202 the Root of Detachment Faults at a Melt-Starved Mid-Ocean Ridge: A Microstructural
203 Study of Abyssal Peridotites From the Southwest Indian Ridge. *Geochemistry,*
204 *Geophys. Geosystems* **22**, e2020GC009434 (2021).
- 205 31. Bickert, M., Lavier, L. & Cannat, M. How do detachment faults form at ultraslow mid-
206 ocean ridges in a thick axial lithosphere? *Earth Planet. Sci. Lett.* **533**, 116048 (2020).
- 207 32. Schlindwein, V. & Schmid, F. Mid-ocean-ridge seismicity reveals extreme types of
208 ocean lithosphere. *Nature* **535**, 276–279 (2016).
- 209 33. Minshull, T. A., Muller, M. R. & White, R. S. Crustal structure of the Southwest
210 Indian Ridge at 66°E: Seismic constraints. *Geophys. J. Int.* **166**, 135–147 (2006).
- 211 34. Meier, M. *et al.* Segment-Scale Seismicity of the Ultraslow Spreading Knipovich
212 Ridge. *Geochemistry, Geophys. Geosystems* **22**, (2021).
- 213 35. Grevemeyer, I. *et al.* Constraining the maximum depth of brittle deformation at slow-
214 and ultraslow-spreading ridges using microseismicity. *Geology* **47**, 1069–1073 (2019).
- 215 36. Tao, C. *et al.* First active hydrothermal vents on an ultraslow-spreading center:
216 Southwest Indian Ridge. *Geology* **40**, 47–50 (2012).
- 217 37. Copley, J. T. *et al.* Ecology and biogeography of megafauna and macrofauna at the
218 first known deep-sea hydrothermal vents on the ultraslow-spreading Southwest Indian
219 Ridge. *Sci. Rep.* **6**, (2016).
- 220 38. Havskov, J. & Ottemöller, L. SeisAn earthquake analysis software. *Seismol. Res. Lett.*
221 **70**, 532–534 (1999).
- 222 39. Baillard, C., Crawford, W. C., Ballu, V., Hibert, C. & Mangeney, A. An automatic
223 kurtosis-based P-and S-phase picker designed for local seismic networks. *Bull.*
224 *Seismol. Soc. Am.* **104**, 394–409 (2014).
- 225 40. Kissling, E., Ellsworth, W. L., Eberhart-Phillips, D. & Kradolfer, U. Initial reference
226 models in local earthquake tomography. *J. Geophys. Res.* **99**, 19635–19646 (1994).
- 227 41. Corbalán, A. *et al.* Seismic Velocity Structure Along and Across the Ultraslow-
228 Spreading Southwest Indian Ridge at 64°30'E Showcases Flipping Detachment Faults.
229 *J. Geophys. Res. Solid Earth* **n/a**, e2021JB022177 (2021).
- 230 42. Lomax, A., Virieux, J., Volant, P. & Berge-Thierry, C. Probabilistic Earthquake
231 Location in 3D and Layered Models. in 101–134 (Springer, Dordrecht, 2000).
232 doi:10.1007/978-94-015-9536-0_5.
- 233 43. Waldhauser, F. & Ellsworth, W. L. A Double-difference Earthquake location
234 algorithm: Method and application to the Northern Hayward Fault, California. *Bull.*
235 *Seismol. Soc. Am.* **90**, 1353–1368 (2000).
- 236 44. Krischer, L. hypoDDpy: hypoDDpy 1.0. (2015) doi:10.5281/ZENODO.18907.
- 237 45. Schweitzer, J. HYPOSAT — An Enhanced Routine to Locate Seismic Events BT -
238 Monitoring the Comprehensive Nuclear-Test-Ban Treaty: Source Location. in (eds.
239 Ringdal, F. & Kennett, B. L. N.) 277–289 (Birkhäuser Basel, 2001). doi:10.1007/978-

3-0348-8250-7_17.

46. Zhao, M. *et al.* Three-dimensional seismic structure of the Dragon Flag oceanic core complex at the ultraslow spreading Southwest Indian Ridge (49°39'E). *Geochemistry, Geophys. Geosystems* **14**, 4544–4563 (2013).
47. Niu, X. *et al.* Along-axis variation in crustal thickness at the ultraslow spreading Southwest Indian Ridge (50°E) from a wide-angle seismic experiment. *Geochemistry, Geophys. Geosystems* **16**, 468–485 (2015).
48. Jian, H. *et al.* Seismic structure and magmatic construction of crust at the ultraslow-spreading Southwest Indian Ridge at 50°28'E. *J. Geophys. Res. Solid Earth* **122**, 18–42 (2017).
49. Zhao, D., Hasegawa, A. & Horiuchi, S. Tomographic imaging of P and S wave velocity structure beneath northeastern Japan. *J. Geophys. Res.* **97**, (1992).
50. Richter, C. F. An instrumental earthquake magnitude scale. *Bulletin of the Seismological Society of America* vol. 25 1–32
<https://pubs.geoscienceworld.org/ssa/bssa/article-abstract/25/1/1/115102/An-instrumental-earthquake-magnitude-scale> (1935).
51. Anderson, J. A. & Wood, H. O. Description and theory of the torsion seismometer. *Bull. Seismol. Soc. Am.* **15**, 1–72 (1925).
52. Illsley-Kemp, F. *et al.* Local earthquake magnitude scale and b-value for the Danakil region of northern afar. *Bull. Seismol. Soc. Am.* **107**, (2017).
53. Keir, D., Stuart, G. W., Jackson, A. & Ayele, A. Local earthquake magnitude scale and seismicity rate for the Ethiopian rift. *Bull. Seismol. Soc. Am.* **96**, (2006).
54. Hardebeck, J. L. & Shearer, P. M. A new method for determining first-motion focal mechanisms. *Bull. Seismol. Soc. Am.* **92**, (2002).
55. Snoke, J., Munsey, J., Teague, A. & Bollinger, G. A program for focal mechanism determination by combined use of polarity and SV-P amplitude ratio data. *Earthq. notes* **55**, 15 (1984).
56. Cannat, M. *et al.* A forest of carbonate-brucite chimneys at the Southwest Indian Ridge: the ultramafic-hosted Old City hydrothermal field. in *Goldschmidt Conference Abstract* (2019).

Methods

Microearthquake experiments

The first experiment, using 14 OBSs in a cross configuration, recorded 8 days of microearthquakes in between airgun shots during the SISMOSMOOTH active seismic survey in October 2014 (R/V *Marion Dufresne*; SMSMO catalog; Fig. 1). The second experiment, using 6 OBSs in a hexagon configuration, continuously recorded 19 days of microearthquakes during the ROVSMOOTH cruise in December 2016 (R/V *Pourquoi Pas?*;

RVSMO catalog; Fig. 1). Each OBS recorded three orthogonal ground motions plus pressure signals.

Earthquake detection

The internal clocks of the OBSs were synchronized on deployment and recovery, and a linear drift correction was applied. Earthquake events were detected by the CONDET program in the SEISAN software³⁸, and an automatic picking procedure³⁹ was used to pick P and S wave arrival onsets. These events were registered in the SEISAN database, and P- and S-wave arrival onsets were manually refined (Extended Data Fig. 1).

1-D velocity model

The 1-D P-wave velocity model was calculated using the VELEST program⁴⁰. The initial velocity model was extracted from a seismic refraction experiment across DF1 during the SISMOSMOOTH cruise²², which is in general agreement with a broader velocity model at the same area⁴¹ (Extended Data Fig. 2). Only events with $OBS \geq 6$ and $GAP \leq 180^\circ$ were used in the VELEST program. The best-fitting P-wave velocity model was iteratively searched (Extended Data Fig. 2). The final root-mean-square (RMS) is acceptable low at 107 ms. The S-wave velocity (V_s) model is calculated using a best-fitting V_p/V_s ratio of 1.7 (ranging from 1.5 to 2.1), based on the Wadati diagram that plots travel time of P-wave versus travel time differences of P- and S- waves (S-P time; Extended Data Fig. 3).

Earthquake location and relocation

The initial earthquake locations were searched by the NonLinLoc software with the Oct-tree algorithm⁴² and the SWIR 64°30'E velocity model (Extended Data Fig. 2). 402 events of SMSMO (92) and RVSMO (292) catalogs were located with four or more stations (Supplementary Figs. 1a-1 to 1d-1). Station corrections were applied for the P and S phases (Extended Data Fig. 4), and the mean absolute station correction is only 60 ± 40 ms in both

catalogs. P- and S-waves travel time residuals follow the Gaussian distribution with an average RMS misfit of 34 ms (Supplementary Fig. 2).

We also applied the SWIR 65-66°E velocity model³² (Extended Data Fig. 2), derived from a more magmatically-robust area than our study area^{22,33}, to locate earthquakes recorded in our study area using the NonLinLoc software (Supplementary Figs. 1a-2 to 1d-2). Earthquakes with more distant epicenters to the OBS network tend to have deeper hypocenters to form an inverted V shape of along-axis hypocenter depth distribution (Supplementary Figs. 1b-2), which is similar to what was documented at the SWIR 65-66°E³².

309 events, with horizontal and depth errors of <5 km and RMS residual of <100 ms, were relocated using the Double-Difference Hypocenter (HypoDD) algorithm⁴³. The relocation uses both catalog and cross-correlation (Supplementary Figs. 3a-3 to 3d-3) and runs using the python module HypoDDpy⁴⁴. A time window of 300 ms was applied based on pickings of P and S arrival onsets, and a correlation coefficient lower than 0.6 was rejected in cross-correlation. We also tested catalog only (Supplementary Figs. 3a-1 to 3d-1) and cross-correlation only (Supplementary Figs. 3a-2 to 3d-2) in HypoDD algorithm, which show stable seismicity patterns for both SMSMO and RVSMO catalogs and the improvement after relocation with applying both catalog and cross-correlation.

The 18 km-thick seismogenic lithosphere at the Dragon Flag detachment system of the SWIR^{26,27} is derived from two different microearthquake catalogs. The early one²⁷ recorded 17.5 days on average of microearthquakes in between airgun shots in 2010 (similar to the SMSMO catalog). Hypocenters were located using the least-squares HYPOSAT routine⁴⁵ with a 1-D velocity model (an average value taken from several active-source tomography velocity models⁴⁶⁻⁴⁸) and relocated using the Tomog3D⁴⁹ with a 3-D velocity model²⁷. The V_p/V_s ratio was assumed as $\sqrt{3}$ ²⁷. 214 well-located earthquake hypocenters have depths between 0 and 18 km bsf²⁷. The late one²⁶ recorded more than 9 months in total of

microearthquakes during three different cruises in 2015-2017. Hypocenters were also located using the HYPOSAT routine⁴⁵ with a 1-D velocity model taken from ref.⁴⁶ but relocated using the HypoDD algorithm⁴³ with the same velocity model. The V_p/V_s ratio was not provided²⁶. 512 well-located earthquake hypocenters have a maximum depth of 13 ± 2 km²⁶. We adopt the maximum depth (18 km) of two earthquake catalogs in the discussion.

Earthquake magnitude calculation

The definition of local magnitudes (M_L) is given by⁵⁰:

$$M_L = \log(A) + n \log(r) + K r + C,$$

where A (in nm) is the maximum amplitude of horizontal components picked in the Wood-Anderson seismogram⁵¹, r (in km) is the hypocentral distance, C is a correction for each OBS, and n and K are constants to be calculated and related to geometrical spreading and attenuation of seismic waves, respectively. The local magnitudes, parameters n and K , and station correction can be solved by a least-squares criterion that produces an optimal solution^{52,53}. For the SMSMO and RVSMO catalogs together, we obtain $n = -2.923$ and $K = 5.85 \times 10^{-3}$.

First-motion focal mechanism

To calculate best-fitting focal mechanisms, we use two first-motion-based algorithms, HASH⁵⁴ and FOCMEC⁵⁵. Multiple criteria were applied: apparent first-motion polarities of P-wave onsets ≥ 8 , azimuthal gaps $\leq 250^\circ$, the weighted fraction of misfit polarities $< 10\%$, RMS of fault plane uncertainty from HASH $\leq 35^\circ$, and similar reasonable solutions generated by both approaches. Eight acceptable focal mechanisms were found in the SMSMO catalog (Fig. 2). We did not obtain focal mechanisms in the RVSMO deployment due to the lesser number of OBSs.

350 **Acknowledgments**

351 We thank the crews of the RVs *Marion Dufresne* and *Pourquoi Pas?* for collecting the data.
352 We also thank Zhiteng Yu, Soumya Bohidar, and Aude Lavayssière for their help in the data
353 processing. We thank the funding of the ANR project "Ridge-Factory-Slow" (ANR-18-
354 CE010002-01). Jie Chen was supported by the China Scholarship Council (201808330437).
355 This is IGP contribution #4239.

356 **Author contributions**

357 J.C. processed the microseismicity data and wrote the manuscript. W.C. supervised J.C. data
358 processing, interpretation, and writing. M.C. developed the project, participated in the
359 SISMOSMOOTH and ROVSMOOTH cruises, led the data collection, and supervised J.C.
360 interpretation and writing.

361 **Competing interests**

362 The authors declare no competing interests.

363 **Data availability**

364 OBS locations, two earthquake catalogs, swarm events, and focal mechanisms are provided
365 in the Supplementary Information.

366

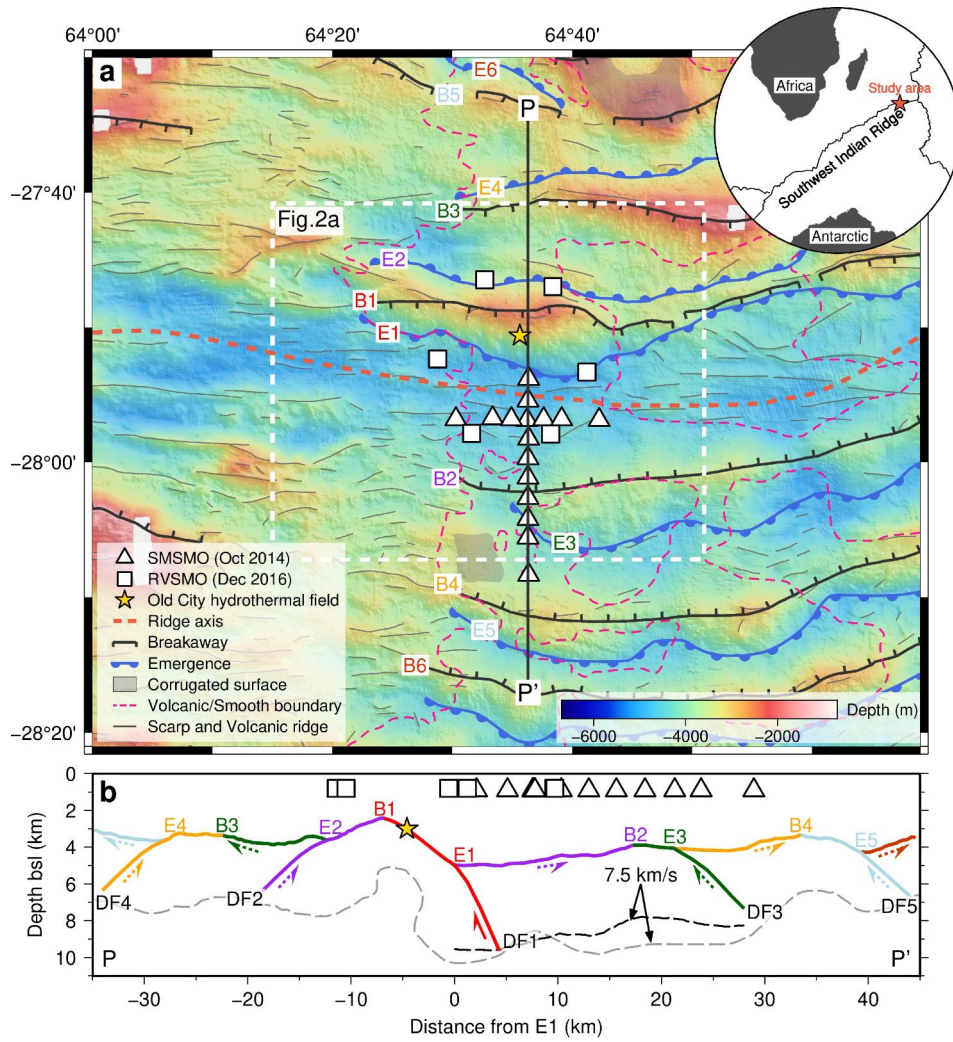


Fig. 1 | OBS locations and tectonic interpretation of the flip-flop detachment fault system at the eastern SWIR. (a) Tectonic map with locations of the OBS networks: SMSMO (14 OBSs in triangles) and RVSMO (6 OBSs in squares). Geological and tectonic information (see legend for symbols) includes breakaways (B1-B6) and emergences (E1-E6) of successive detachment faults, corrugated surface, the boundary between volcanic and smooth seafloor, and linear sketches of scarps and volcanic ridges¹. Yellow star is the Old City hydrothermal field⁵⁶. White dashed square marks the bounds of Fig. 2a. **(b)** Tectonic interpretation of the successive flip-flop detachment fault system along the PP' cross-section¹. Black²² and gray⁴¹ dashed lines are the 7.5 km/s velocity contours. Locations of OBSs are projected to the PP' cross-section. bsl: below sea level.

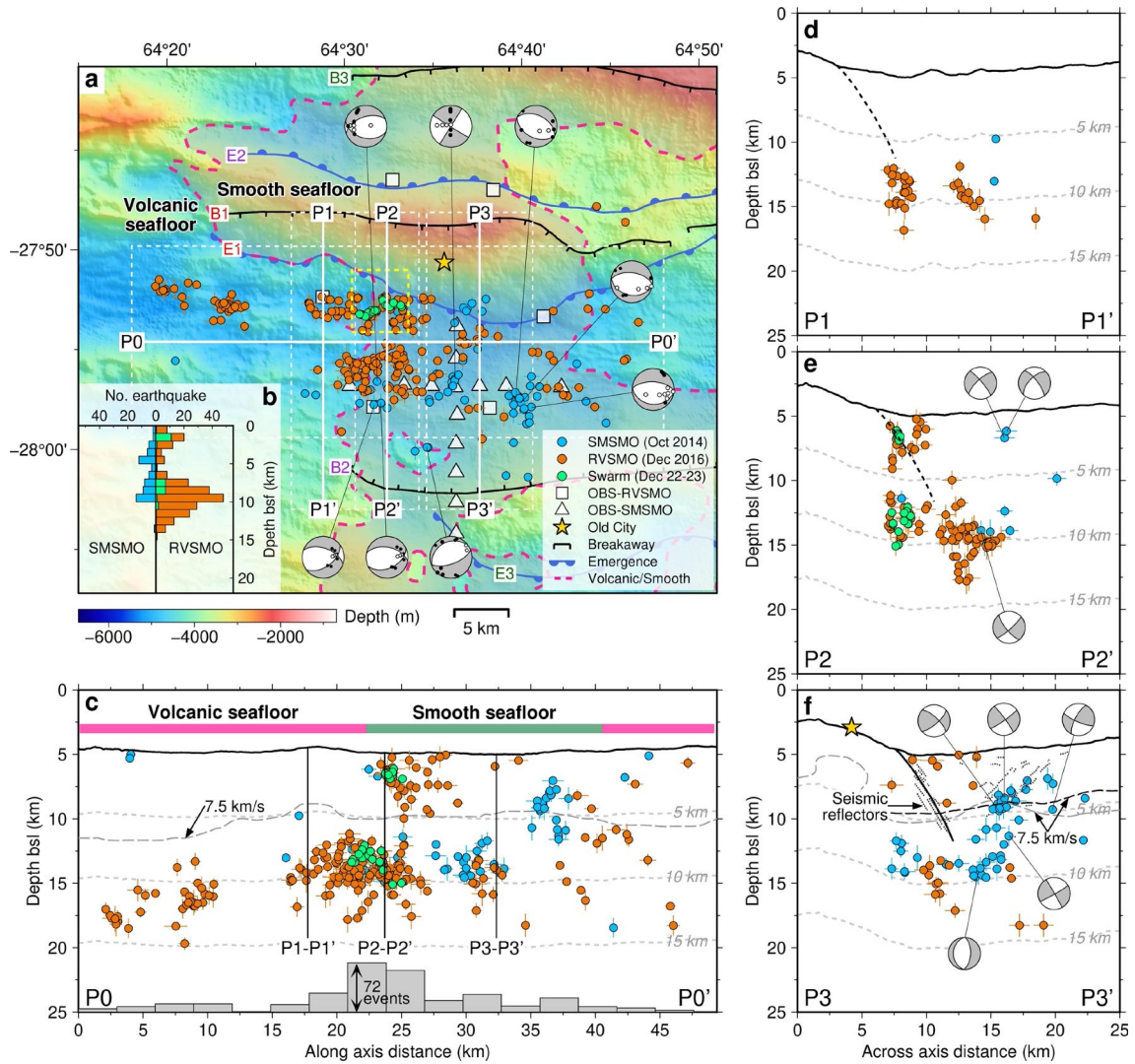


Fig. 2 | Distribution of earthquakes and focal mechanisms. (a) Bathymetric map of the SWIR 64°30'E area showing the events of the SMSMO (blue circles) and RVSMO (orange circles) catalogs, the RVSMO seismic swarm (green circles), and all determined focal mechanisms. Geological information (see legend for symbols) includes breakaways, emergences, and the boundary between volcanic and smooth seafloor¹. Best-fitting focal mechanisms have clear upward (black dots) and downward (white dots) first motions of P-wave onsets (Methods). Depth profiles (P0-P0' to P3-P3') are marked as labelled white lines in Fig 2a, with white dashed squares showing the corresponding boundaries for projected earthquakes in Figs. 2c-2f. Yellow dashed square in Fig. 2a marks the location of Fig. 3b. (b) Histograms of earthquake depths below seafloor for the SMSMO (blue) and RVSMO

(orange) catalogs, including the seismic swarm (green). (c) Along-axis depth profile P0-P0' projecting earthquakes within ± 8 km off the profile ($VE=1$ and the same below). The classification of volcanic (pink) and smooth (green) seafloor is indicated⁴. Gray dashed line is the 7.5 km/s velocity contour⁴¹. Labelled gray dashed lines show depths below the seafloor (the same below). (d) and (e) Across-axis depth profiles P1-P1' and P2-P2' projecting earthquakes within ± 3 km off the profiles. Black dashed lines indicate the fault plane adapted from Fig. 2f. (f) Across-axis depth profile P3-P3' projecting earthquakes within ± 5 km off the profile. Dotted lines represent seismic reflectors, interpreted as DF1 damage zone²², with the main detachment fault plane tentatively drawn in the center (subseafloor solid black line). Black²² and gray⁴¹ dashed lines are the 7.5 km/s velocity contours. Focal mechanisms are projected to profiles P2-P2' and P3-P3'.

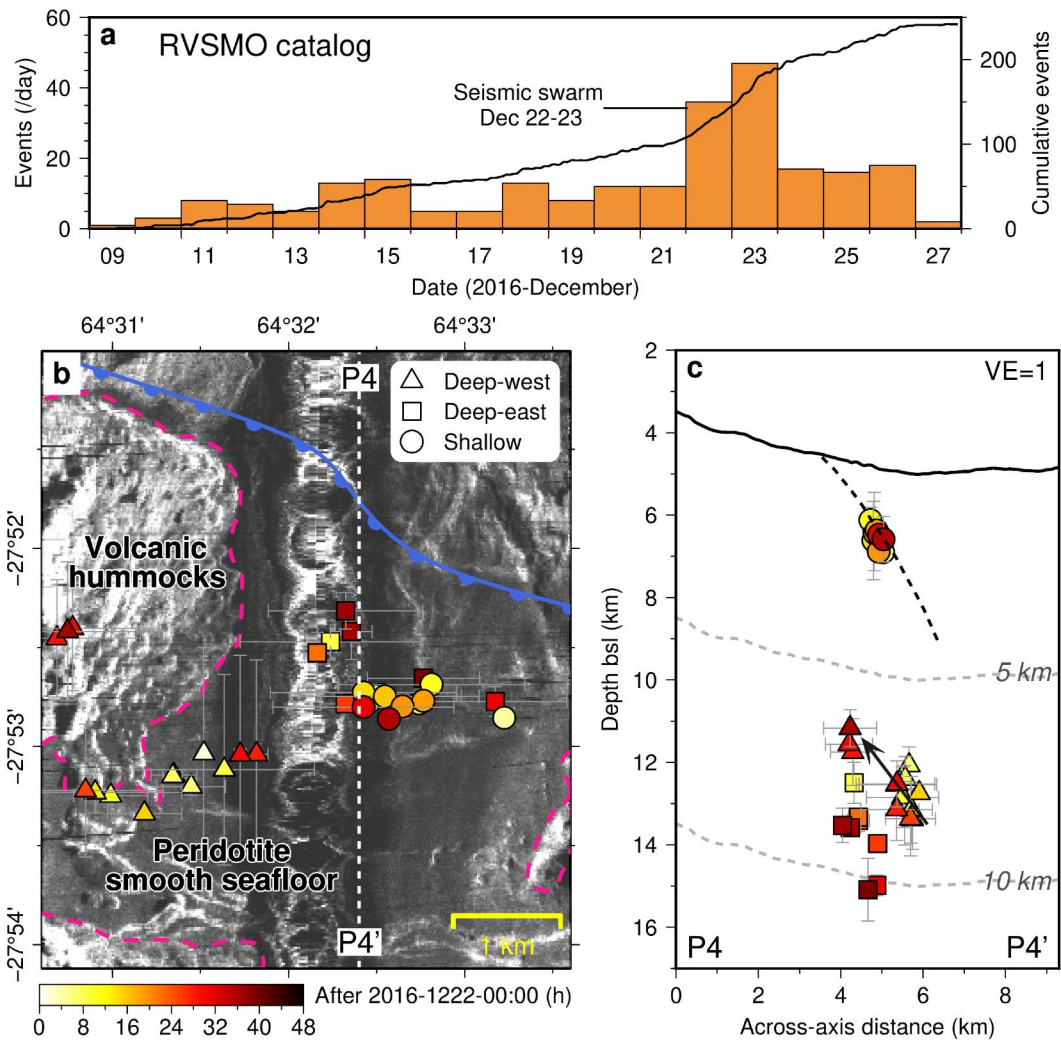
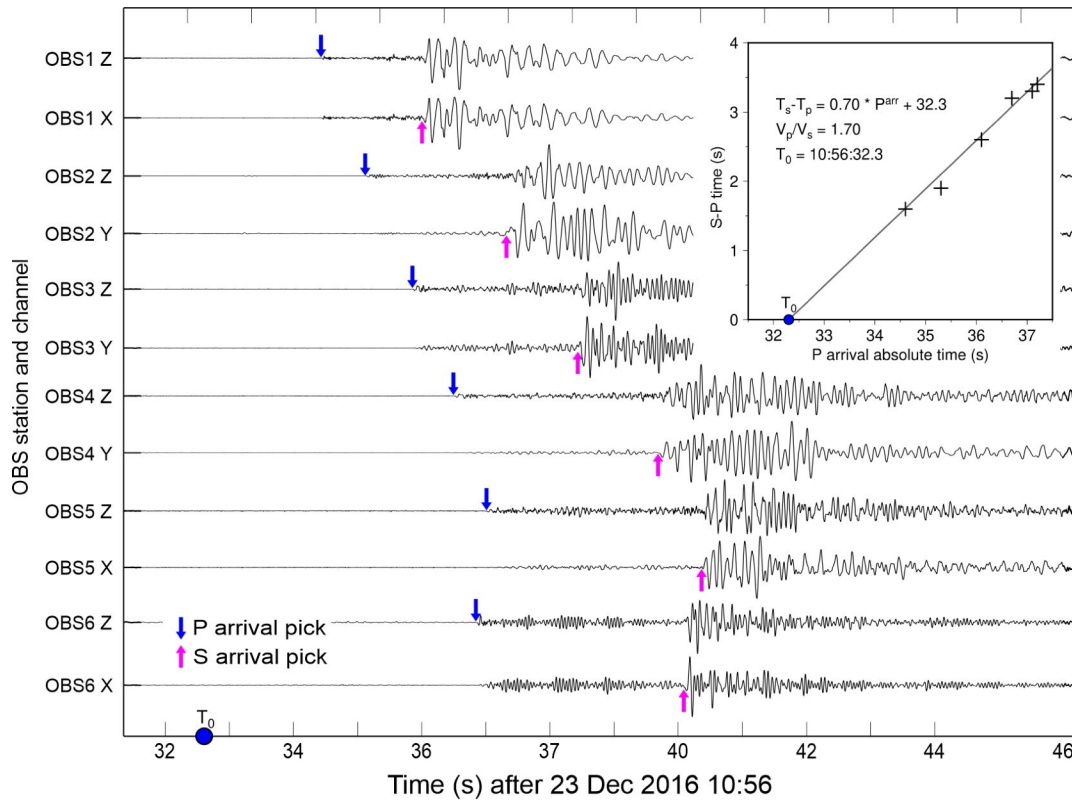
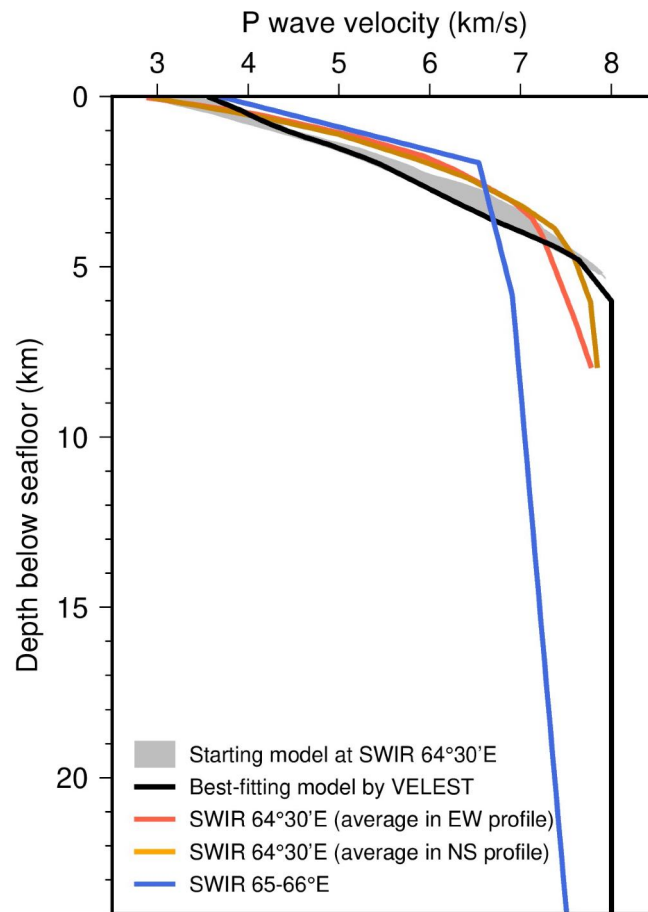


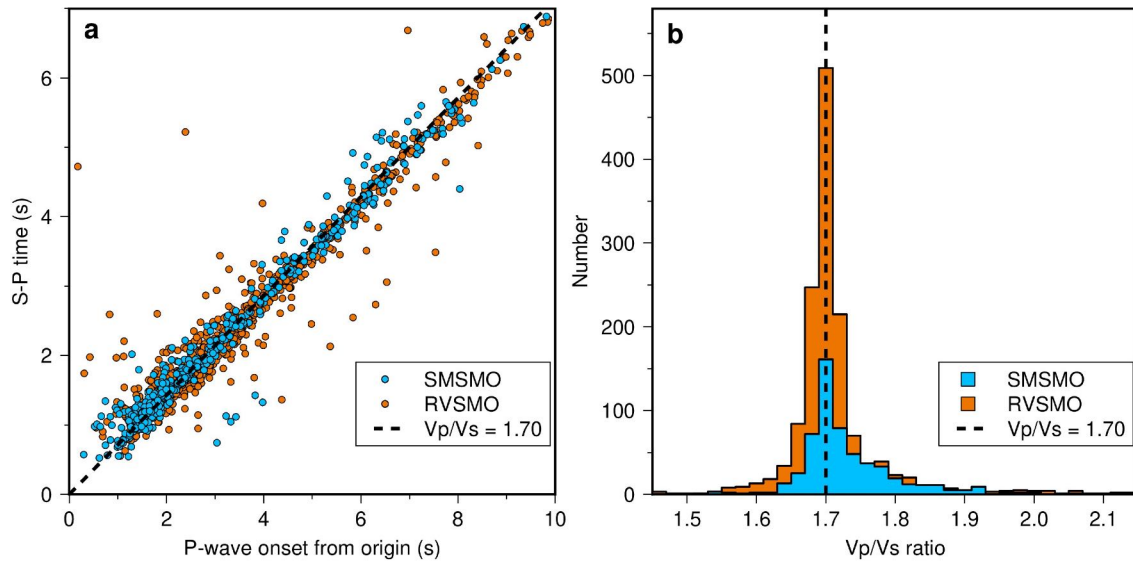
Fig. 3 | Temporal and spatial distribution of the seismic swarm. (a) Histogram and cumulative histogram of located earthquakes for the RVSMO catalog. A seismic swarm with a total of 34 earthquakes occurred during December 22-23, 2016. **(b)** Epicenters of the seismic swarm, superimposed on the map of seafloor reflectivity showing the distribution of volcanic hummocks (dashed pink line on less reflective peridotite smooth seafloor²). The swarm earthquakes are divided into three clusters: deep-west (triangles), deep-east (squares), and shallow (circles). Fill color of symbols indicates the time after 00:00, December 22nd, 2016. **(c)** Across-axis depth profile P4-P4' (dashed white line in Fig. 3b) with projected swarm earthquakes (VE=1). Arrow indicates upward migration over time for the deep-west cluster. Black dashed line shows detachment fault as in Fig. 2e. Labelled gray dashed lines show depths below the seafloor.



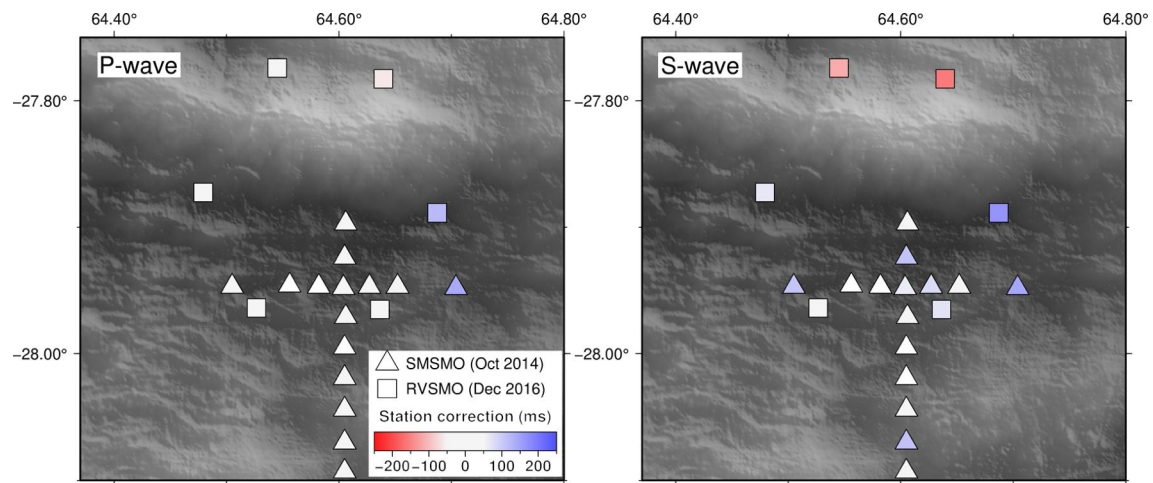
Extended Data Fig. 1 | Typical event waveforms. The event occurred at 64.394°E/27.883°S 11.6 km below seafloor with a local magnitude of 2.3, at 10:56, 23 Dec 2016 in RVSMO catalog. The inset shows the P-wave arrival absolute time versus arrival time differences of P- and S-waves (S-P time), yielding the origin time (T_0) of 10:56:32.3 and a V_p/V_s ratio of 1.7.



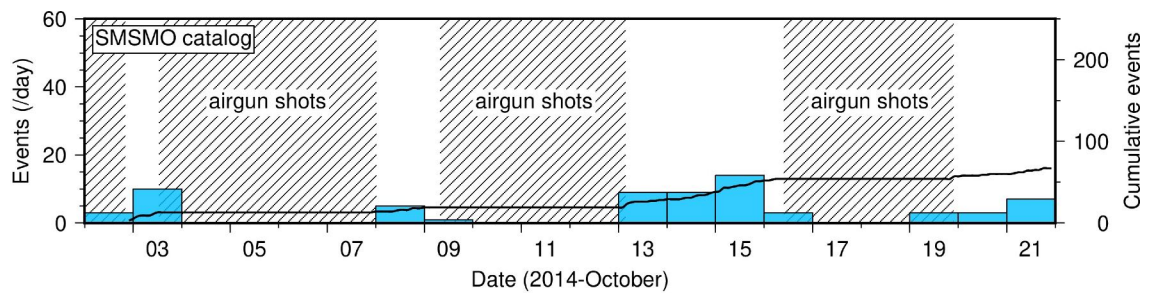
Extended Data Fig. 2 | 1-D P wave velocity model. Starting model (gray area) at the SWIR 64°30'E is extracted from a seismic refraction experiment²². The best-fitting model (black line) is iteratively searched by the VELEST program⁴⁰. Red and orange lines are average velocity models in EW and NS profiles at the SWIR 64°30'E⁴¹. Blue line is the velocity model at the SWIR 65-66°E³².



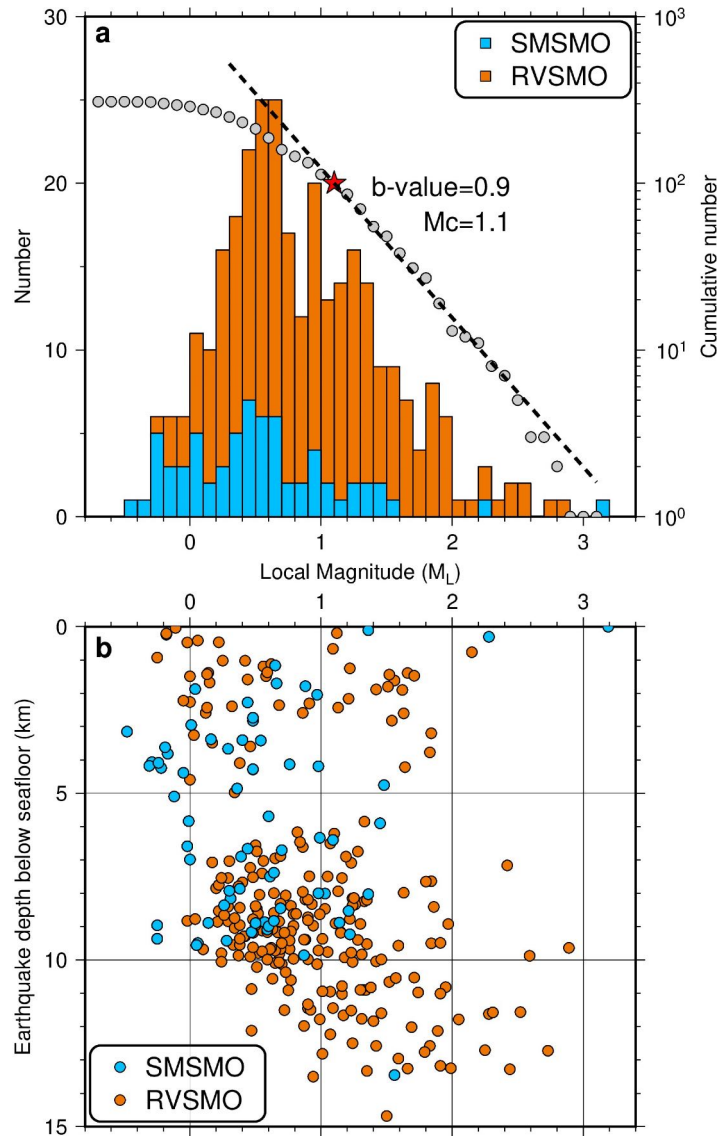
Extended Data Fig. 3 | Wadati diagram. (a) P-wave onset from origin versus S-P time (Wadati diagram) for both SMSMO (orange) and RVSMO (blue) catalogs. **(b)** Histogram of V_p/V_s ratio. V_p/V_s ratio is calculated from the slopes of the Wadati diagram. The best-fitting V_p/V_s ratio is 1.7.



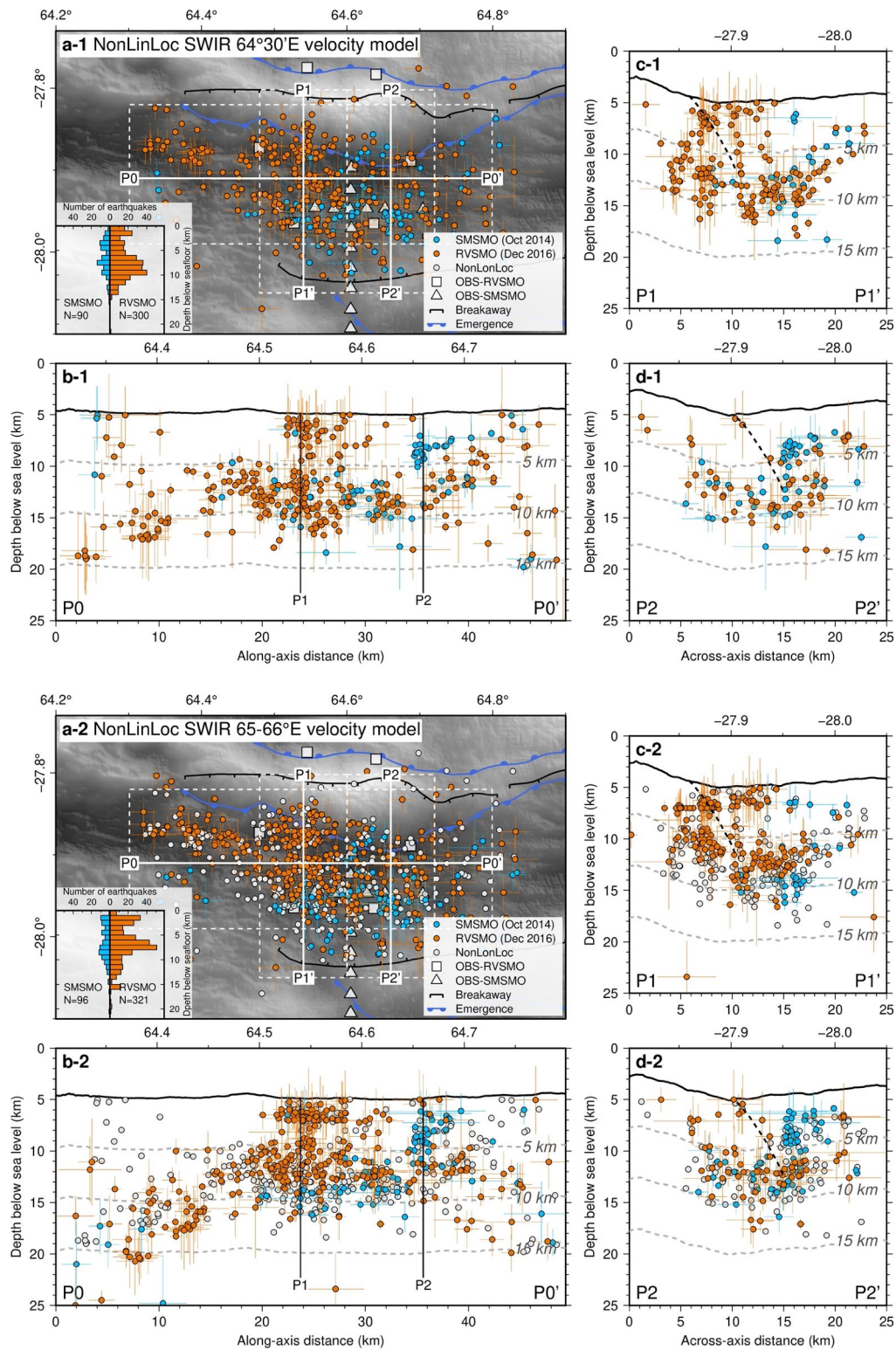
Extended Data Fig. 4 | Station corrections of P- and S-wave returned by NonLinLoc.



Extended Data Fig. 5 | Histogram and cumulative histogram of located earthquakes for the SMSMO catalog.

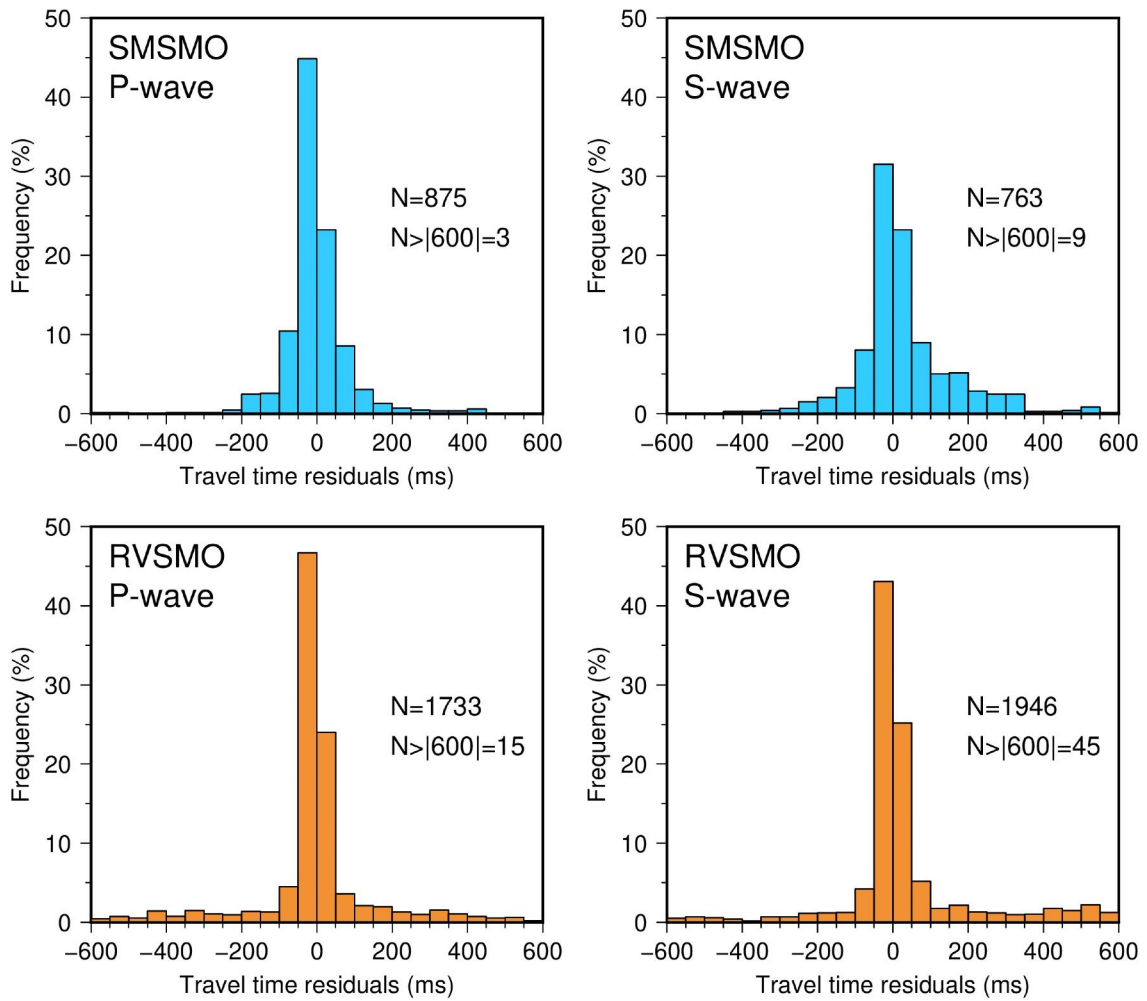


Extended Data Fig. 6 | Distribution of local magnitude (M_L). (a) Histograms of local magnitude for the SMSMO (blue) and RVSMO (orange) catalogs (left Y-axis). The cumulative number of earthquakes for both catalogs (gray circles) as a function of local magnitude (right Y-axis). Magnitude completeness (M_c) is determined as 1.1 (red star), resulting in a b-value of 0.9 (slope of the dashed line). (b) Local magnitude as a function of earthquake depth for the SMSMO (blue) and RVSMO (orange) catalogs.



448

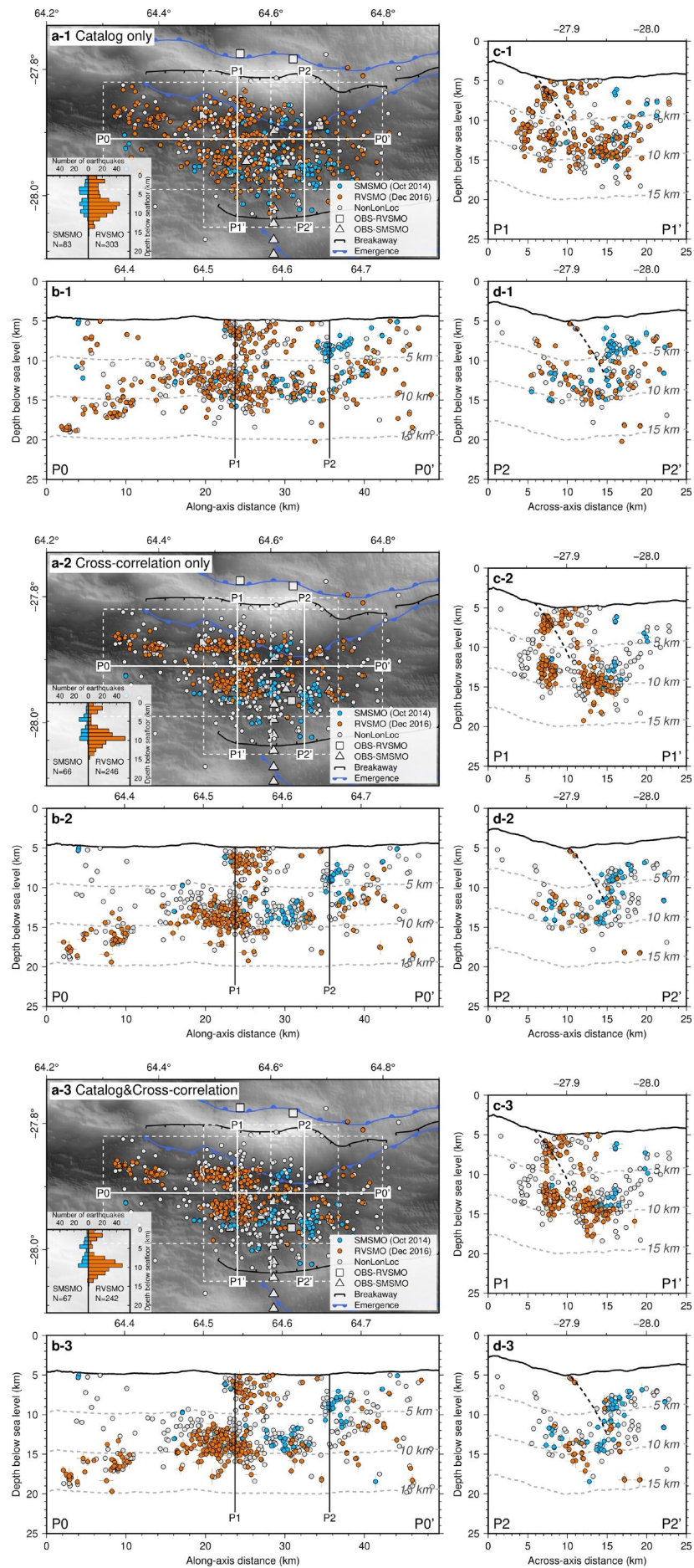
449 **Supplementary Fig. 1 | Earthquake locations.** See legend for symbols. Earthquake
 450 locations using the NonLinLoc with the SWIR 64°30'E velocity model (a-1 to d-1).
 451 Earthquake locations using the NonLinLoc with the SWIR 65-66°E velocity model (a-2 to d-
 452 2), compared with the NonLinLoc results with the SWIR 64°30'E velocity model (pale gray).
 453 Velocity models see Extended Data Fig. 2.



454

455 **Supplementary Fig. 2 | Frequency distribution of P- and S-wave travel time residuals**

456 **for the SMSMO (blue) and RVSMO (orange) catalogs.**



458 **Supplementary Fig. 3 | Earthquake relocations.** See legend for symbols. Tests of
459 earthquake relocation using the HypoDD with catalog only (**a-1** to **d-1**), cross-correlation
460 only (**a-2** to **d-2**), and catalog&cross-correlation (**a-3** to **d-3**; same results as Fig. 2). All are
461 compared with the NonLinLoc results (pale gray) with the SWIR 64°30'E velocity model
462 (Supplementary Figs. 1a-1 to 1d-1).

Supplementary Files

This is a list of supplementary files associated with this preprint. Click to download.

- [SupplementaryInformation.zip](#)